Journal of Japan Society of Civil Engineers, Ser.
B1 (Hydraulic Engineering), Vol. 67, No. 4, I_181-I_186, 2011.

THREE-DIMENSIONAL SIMULATION OF FLOW AT AN OPEN-CHANNEL CONFLUENCE WITH TURBULENCE MODELS

Mung DINH THANH[1], Ichiro KIMURA[2], Yasuyuki SHIMIZU[3]

[1]Student Member of JSCE, Graduate Student, Hydraulic Research Laboratory, Hokkaido University (Sapporo 060-8623, Kita-ku, Kita-13, Nishi-8, Japan)
[2]Member of JSCE, Dr. of Eng., Associate Professor, Hydraulic Research Laboratory, Hokkaido University (Sapporo 060-8623, Kita-ku, Kita-13, Nishi-8,Japan)
[3]Member of JSCE, Dr. of Eng., Professor, Hydraulic Research Laboratory, Hokkaido University (Sapporo 060-8623, Kita-ku, Kita-13, Nishi-8, Japan)

Open-channel confluence flows are common in natural river systems as well as in environmental and hydraulic engineering, such as in river engineering. Often, these flows are three-dimensional and complex, while numerical studies fully describing confluence flow are still few. This paper presents the results of investigation of confluence flow using a three-dimensional numerical model with the linear and nonlinear k-ε models. To treat the dynamic boundary condition at the free surface, non-hydrostatic pressure is included in the present model. The model is validated using the experimental data available. Adequacy of the present model with two turbulence models above is indicated based on the result analysis. The nonlinear model is indicated as the more advantageous one than the linear one.

Key Words: *open channel confluence, 3D model, k-ε model, secondary current*

1. INTRODUCTION

Open-channel confluence flows are often encountered in nature as well as in environmental and hydraulic engineering. Detailed hydrodynamics of confluence flow is found to be complex and influenced by a number of parameters, including the size, shape, slope, junction angle, and the flow Reynolds and Froude numbers. Flow structure at an open-channel confluence has a great influence on sediment transport and channel evolution, including the bed erosion, deposition, and transport and diffusion of contaminated matters. However, this flow is highly three-dimensional and simulation, which reflects all characteristics of the flow in a confluence, is not a straightforward work.

In the past, a number of studies of confluence flows have been conducted using physical models, one-dimensional theoretical analysis, or one-dimensional numerical models, such as works of Best and Reid[1)], Gurram et al.[2)], and Hsu et al.[3), 4)]. These studies provided insightful information to the understanding of confluence flow. However, simplified theoretical or one-dimensional numerical models are less capable of considering complicated flow conditions, for instance, secondary current and separation.

In order to overcome limitations of the one-dimensional models, two-dimensional numerical models are developed and applied to open-channel confluence flow. Cheng et al.[5)] numerically simulated the two-dimensional T-type confluence flow using the standard k-ε model and its other versions (low-Reynolds number, improved k-ε model proposed by Hanjalic and Launder). Their results indicated the reasons of the unsatisfactory prediction using these models. One main reason is exclusion of secondary current effect due to streamline curvature. Attempts to advance the two-dimensional model for prediction of confluence flow are done by Dinh et al.[6)]. In these studies, the authors presented application of four various types of the depth-averaged two-dimensional models to this flow with and without considering secondary current of the first kind due to streamline curvature. The results obtained by the models with effects of secondary current shown superiority of them over the model excluding this flow in term of prediction of average velocity profile and field, water surface elevation, and secondary pattern profile. However, these advanced depth-averaged models did not well predict secondary currents because of highly three-dimensional feature as well as complex nature of confluence flow. Recently, Uchida and Fukuoka[7] developed a quasi-3D model using shallow water equations and horizontal vorticity equations to compute a flow in channel confluences. However, the separation size and the water surface depression zone for the case of more flow coming from the branch than that from the main channel were over-predicted in comparison with the measured results.

Three-dimensional computational model is an appropriate approach to investigate all confluence flow characteristics. As well as two-dimensional numerical model, there were a few of studies using three-dimensional numerical model to address with the confluence flow. Huang et al.[8] developed and validated a three-dimensional numerical model in order to investigate the effect of junction angle on the confluence flow. In their study, hydrostatic pressure was assumed and the k-ω turbulence model was used to calculate the turbulence eddy viscosity. The results obtained with this model were fair. However, there are some points that do not agree well with the experimental results, including secondary currents, the width of separation zone, and water surface elevation profiles in the separation region. Therefore, this model is appropriate to some extent.

The purpose of this paper is to present a three-dimensional numerical simulation using the linear and nonlinear k-ε models. Governing equations and two equations of the turbulence model are written in a moving boundary-fitted coordinate. Non-hydrostatic pressure is used in this study. The computed results are compared to the experimental results of Weber et al.[9] for validation, and then adequacy of the models are discussed based on this comparison.

2. COMPUTATIONAL MODEL

(1) Governing equations

In this study, the unsteady Reynolds-Averaged Navier-Stokes equations are used. In a moving boundary-fitted coordinate, they are written as follows.

a) Continuity equation

$$\frac{1}{\sqrt{g}}\frac{\partial V^{\alpha}\sqrt{g}}{\partial \xi^{\alpha}}=0 \tag{1}$$

b) Momentum equations

$$\frac{\partial V^i}{\partial t}+\nabla_j\left[V^i(V^j-W^j)\right]+V^i\nabla_j W^j+V^j\nabla_j W^i = F^i-\frac{1}{\rho}g^{ij}\nabla_j p+\nabla_j\left[-\overline{v^i v^j}\right]+2\nu\nabla_j S^{ij} \tag{2}$$

where t=time; V^i=contravariant components of velocity; W^i=contravariant components of mesh velocity; v^i=turbulent flow velocity vector; F^i=contravariant components of gravitational vector, p=pressure; g^{ij}=contravariant metric tensor; g=determinant of metric tensor; ρ=fluid density; ξ^i=boundary-fitted coordinates; ν=dynamic viscosity; $-\overline{v^i v^j}$ =Reynolds stress; S^{ij}=contravariant components of strain tensor; and $\nabla_i A^k$ =covariant derivative of contravariant vector, A^k, and is defined as

$$\nabla_i A^k=\frac{\partial A^k}{\partial \xi^j}+A^j\Gamma^k_{ij} \tag{3}$$

where Γ_{ij}^k=Christoffel symbol of the second kind defined as

$$\Gamma^k_{ij}=\frac{1}{2}g^{km}\left(\frac{\partial g_{jm}}{\partial \xi^i}+\frac{\partial g_{im}}{\partial \xi^j}-\frac{\partial g_{ij}}{\partial \xi^m}\right) \tag{4}$$

Here g_{ij}=covariant metric tensor.

In the linear turbulence model, Reynolds stress is evaluated as Eq. (5), while this term is calculated using Eq. (6) in the nonlinear one, which is proposed by Kimura and Hosoda[10].

$$-\overline{v^i v^j}=2D_t S^{ij}-\frac{2}{3}k\delta^i_s g^{sj} \tag{5}$$

$$-\overline{v^i v^j}=2D_t S^{ij}-\frac{2}{3}k\delta^i_s g^{sj}-\frac{k}{\varepsilon}D_t c_\beta\left[\alpha_1 Q_1+\alpha_2 Q_2+\alpha_3 Q_3\right] \tag{6}$$

where

$$Q_1=S^{i\alpha}g_{\alpha l}\Omega^{lj}+S^{j\beta}g_{\beta l}\Omega^{li} \tag{7a}$$

$$Q_2=S^{i\alpha}g_{\alpha l}S^{lj}-\frac{1}{3}S^{k\alpha}g_{\alpha m}S^{m\beta}g_{\beta k}\delta^i_l g^{lj} \tag{7b}$$

$$Q_3=\Omega^{i\alpha}g_{\alpha l}\Omega^{lj}-\frac{1}{3}\Omega^{k\alpha}g_{\alpha m}\Omega^{m\beta}g_{\beta k}\delta^i_l g^{lj} \tag{7c}$$

$$D_t=C_\mu\frac{k^2}{\varepsilon} \tag{8}$$

In the linear turbulence model, C_μ=0.09. However, in the nonlinear model, the coefficients c_β in Eq. (6) and C_μ in Eq. (8) are evaluated using the model proposed by Ali et al.[11]. They are not constant, but a function of strain parameter, S and rotation one, Ω as follows.

$$C_\mu=C_{\mu 0}\frac{\left(1+c_{ns}S^2+c_{n\Omega}\Omega^2\right)}{1+c_{ds}S^2+c_{d\Omega}\Omega^2+c_{ds\Omega}S\Omega+c_{ds1}S^4+c_{d\Omega 1}\Omega^4} \tag{9}$$

$$c_\beta=\frac{1}{1+m_{ds}S^2+m_{d\Omega}\Omega^2} \tag{10}$$

Here, $C_{\mu 0}$=0.09; S and Ω are strain and rotation parameters, respectively and they are defined as

$$S=\frac{k}{\varepsilon}\sqrt{\frac{1}{2}S^{i\alpha}g_{\alpha j}S^{j\beta}g_{\beta i}} \tag{11}$$

$$\Omega=\frac{k}{\varepsilon}\sqrt{\frac{1}{2}\Omega^{i\alpha}g_{\alpha j}\Omega^{j\beta}g_{\beta i}} \tag{12}$$

The model coefficients, α_1, α_2, and α_3 are calculated using Eq.(13).

$$\alpha_1 = (-C_1 + C_2)/4;\ \alpha_2 = (C_1 + C_2 + C_3)/4; \quad (13)$$
$$\alpha_3 = (-C_1 + C_2 - C_3)/4;$$
$$C_1 = 0.40, C_2 = 0.00, C_3 = -0.13$$

$$S^{ij} = \frac{1}{2}\left(g^{i\alpha}\nabla_\alpha V^j + g^{j\beta}\nabla_\beta V^i\right) \quad (14a)$$

$$\Omega^{ij} = \frac{1}{2}\left(g^{j\alpha}\nabla_\alpha V^i - g^{i\beta}\nabla_\beta V^j\right) \quad (14b)$$

c) k and ε equations

$$\frac{\partial k}{\partial t} + \nabla_j\left[k(V^j - W^j)\right] + k\nabla_j W^j = -g_{il}\overline{v^l v^j}\nabla_j V^i - \varepsilon + \nabla_j\left\{\left(\frac{D_t}{\sigma_k} + \nu\right)g^{ij}\nabla_i k\right\} \quad (15)$$

$$\frac{\partial \varepsilon}{\partial t} + \nabla_j\left[\varepsilon(V^j - W^j)\right] + \varepsilon\nabla_j W^j = -C_{\varepsilon 1}\frac{\varepsilon}{k}g_{il}\overline{v^l v^j}\nabla_j V^i - C_{\varepsilon 2}\frac{\varepsilon^2}{k} + \nabla_j\left\{\left(\frac{D_t}{\sigma_\varepsilon} + \nu\right)g^{ij}\nabla_i \varepsilon\right\} \quad (16)$$

where σ_k=1.0, σ_ε=1.3, $C_{\varepsilon 1}$=1.44, and $C_{\varepsilon 2}$=1.92 are the model constants.

(2) Free surface calculation

In this study, an approach of free surface calculation is employed using the kinematic and dynamic boundary conditions.

a) Kinematic boundary condition

Kinematic boundary condition used here is the hybrid Cartesian/curvilinear approach.

$$\frac{\partial H}{\partial t} + V^1\frac{\partial H}{\partial \xi^1} + V^2\frac{\partial H}{\partial \xi^2} = w \quad (17)$$

where H is height of the free surface; t is time; V^1 and V^2 are contravariant components of flow velocity in ξ^1 and ξ^2 directions, respectively; and w is the Cartesian component of velocity in the z-direction.

b) Dynamic boundary condition

In the previous studies, the hydrostatic pressure is often assumed as considering dynamic boundary condition. However, non-hydrostatic pressure is used in the present work with effect of the surface tension and viscosity considered. The following dynamic boundary condition is adopted (Hodge and Street[12]).

$$P_{s+} - P_{s-} = -2\nu\nabla_3 V^3 + 2M\gamma \quad (18)$$

where P is the total pressure (=hydrostatic pressure (SP) + dynamic pressure (DP)); the subscripts $s+$ and $s-$ indicate the pressure on the upper and lower sides of the free surface; ν is the dynamic viscosity; M is the mean curvature of the free surface and is defined for the ξ^3 surface; γ is the surface tension (=0.0728 N/m); and $\nabla_3 V^3$ is covariant derivative of the contravariant velocity component, V^3 with respect to the ξ^3 direction. Assuming that pressure on the upper side of the free surface is zero and water depth at a lower point of the free surface is small enough to SP assumed to be zero, Eq. (18) is then reduced to Eq. (19).

$$DP = 2\nu\nabla_3 V^3 - 2M\gamma \quad (19)$$

(3) Numerical procedure

The momentum equations and transport equations of k and ε are solved with the conservative finite-volume method base on a fully-staggered grid system. In order to prevent the generation of oscillations and spurious solution in regions of high gradients, a MUSCL-TVD scheme with the MINMOD limiter which has third-order accuracy is applied to the convective terms in the momentum equations and the transport equations of k and ε. The Adams-Bashforth scheme with second-order accuracy in time is used for time integration in each equation. The governing equations are discretized as fully explicit forms and are solved along the time axis step by step. Calculation of pressure field is implemented using a fractional step method coupling with the Highly Simplified Mark and Cell (HSMAC) method.

(4) Boundary conditions

The turbulent kinetic energy, k and its ratio of dissipation, ε at wall are evaluated using a wall function which is evaluated by the log-law. At the boundary inlets, the value of k is chosen to be $(0.05U)^2$ (U=average velocity at each inlet); the level of ε is determined from the value of k at the inlets and Eq. (8) by specifying the ratio D_t/ν=100.

In order to consider effect of the rapid attenuation of turbulence intensities in the vertical direction near the free surface, the following damping function, f_s, is multiplied to the eddy viscosity.

$$f_s = 1 - \exp\left(-B\frac{(H - \xi^3)\varepsilon_s}{k_s^{3/2}}\right) \quad (20)$$

where H=water surface height; B=constant (=10); ξ^3= vertical coordinate; subscript s indicates the value at the free surface layer. The turbulent dissipation rate at the free surface layer, ε_s, is evaluated by the following formula to calculate the secondary currents of second kind.

$$\varepsilon_s = \frac{C_{\mu 0}^{3/4}k_s^{3/2}}{0.4\Delta\xi_s^3},\ (C_{\mu 0} = 0.09) \quad (21)$$

where ξ^3 is same as that in Eq. (20).

3. COMPUTATIONAL CONDITION AND DOMAIN

The 3D model described above is validated by computing one flow case of the experiment of Weber et al.[9], which are shown in Table 1. In this table, Q_m=main channel discharge; Q_b=branch channel

Table 1 Computational conditions.

Case	Q_m (m^3/s)	Q_b (m^3/s)	Q_t (m^3/s)	$q^*=Q_m/Q_t$	H_0 (m)	U_0 (m/s)
1	0.043	0.127	0.170	0.250	0.3054	0.608

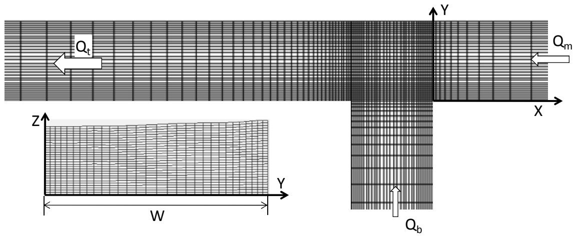

Fig.1 Computational domain and grid.

discharge; Q_t=Total post-confluence channel discharge (=Q_m+Q_b); $q^*=Q_m/Q_t$; H_0 and U_0 are the average water depth and the bulk average flow velocity at the downstream end, respectively.

In the experiment of Weber et al.[9], the channel consists of a main channel of 21.946 m in length and a branch channel of 3.658m in length, which locates 5.484 m downstream of the entrance of the main channel. Both channels have the same with (W) of 0.914 m. However, the computational domain is chosen as follows. The length of post-confluence channel is shorten to 7W (6.398 m) where the water depth, H_0, is nearly constant as shown in Table 1, while the main channel length upstream of the branch channel is prolonged to 12W (10.968 m), and the branch channel length is lengthened to 10W (9.14 m).

A grid independence study has been conducted to determine the appropriate grid point number. The final grid chosen has 92×55×29 cells with a total of 146,740 cells. The computational grid around the junction is shown in Fig. 1.

4. RESULTS AND DISCUSSIONS

(1) Turbulence kinetic energy

Generation of turbulence of the present model after an almost steady state is evaluated through comparison of the calculated turbulence kinetic energy to the experimental one. Here, both are normalized by U_0^2. The distance is normalized by the channel with, W, named as x/W, y/W and z/W. The calculated result at z/W=0.278 (near the water surface) is used for this comparison as shown in Fig. 2. It can be seen that the two models fairly generates general tendency of turbulent region. However, the linear turbulence model under-predicts too much turbulence along the boundary of the passing flow, while the position of the highest turbulent region is not correctly predicted. In contrast, the result with the nonlinear turbulence model is agreeable with the measured one: the highest turbulent region is reasonably reproduced.

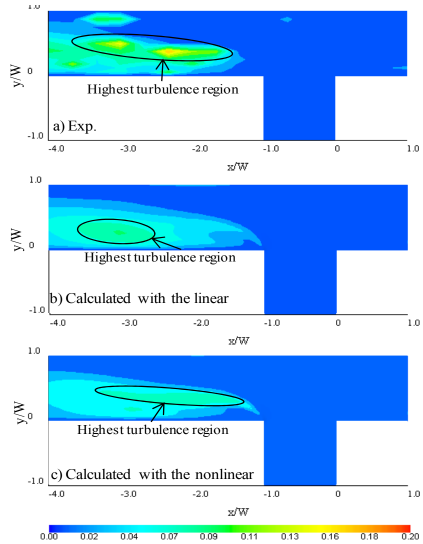

Fig. 2 Comparison of dimensionless turbulence energy (k) by the models with the experimental one at z/W = 0.278.

This difference is because the anisotropy of turbulence and effect of the strain and rotation parameters on the eddy viscosity (D_t) through C_μ are included in the nonlinear model, which are not considered in the linear one.

(2) Water surface elevation

Water surface is normalized with the channel width (W). Fig. 3 displays calculated water surface contours by the linear and nonlinear turbulence models, Figs. 3b and 3c, respectively together with the experimental one. It can be observed that the predicted results agree well with the measured ones. Quantitatively, the predicted minimum dimensionless water surface elevations in the separation zone are 0.306 and 0.308 with the linear and nonlinear models, respectively. These values are very close to the experimental one of 0.306. In comparison with the previous study results (for example, Huang et al.[8]), the present predicted results are better in terms of water-surface mapping and the minimum water surface elevation (this minimum elevation predicted with Huang et al.[8] is 0.311). The main reason may be attributed to non-hydrostatic pressure considered and effect of surface tension and viscosity is taken into account in evaluating dynamic boundary condition.

(3) Flow velocity field

Flow velocity components are normalized by U_0, named as u*, v* and w*. Two velocity fields, one near the water surface and another near the bed, are performed together with those of the experiment in order to assess the prediction of the present 3D model with the linear and nonlinear turbulence models as shown in Figs 4 and 5, respectively.

It can be observed that the critical features of the junction flow are captured with the present 3D model. There is a significant difference between the surface lateral flow and the bed one. The surface lateral flow

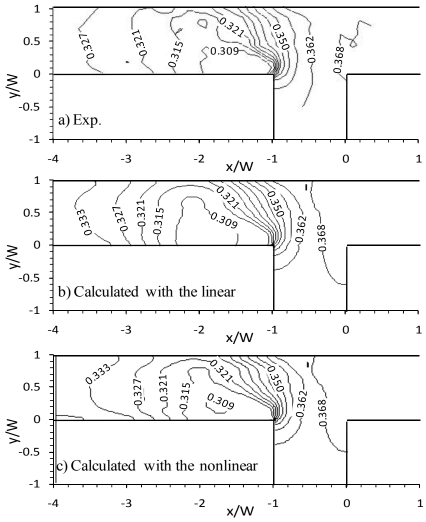

Fig. 3 Comparison of water surface contours.

enters at a larger deflection angle to the main channel in comparison with the bed flow. The larger angle of entry results in a higher momentum at the surface, leading to a wider separation zone at the near surface depths than at the near bed. Another important feature observed is that the surface flow is skewed toward the outer bank, while the bed one is deflected toward the inner bank in the downstream of the confluence when looking downstream. This implies different sediment transport tendencies at the surface and the bed.

Figs 4 and 5 both show that there is a separation zone where reverse velocity occurs downstream of the junction and its size is significantly different between the surface and the bed: The separation zone is larger near the surface than near the bed. Both the results with the linear turbulence model and the nonlinear one generally agree with the experimental results. However, the separation zones generated with the linear model are over-predicted, especially at the bed. The experiment shows the dimensionless lengths of the separation zone at the surface and at the bed are about 2.0 and 1.3, respectively, while those with the linear model are about 2.2 and 1.7. When the nonlinear model is used, these results are significantly improved and reasonably agreeable with the measured ones. These lengths are about 1.9 and 1.4, respectively. The size of the separation zone is influenced by interaction between the passing flow and the flow in the separation. This interaction results in a decrease in momentum of the flow in the boundary region of the separation. Depending on this decrease, the length of the separation zone may be longer or shorter. As indicated above, the linear turbulence model under-predicts turbulence along the boundary of the separation. This implies that decrease in momentum in this region is under-predicted in comparison with that in the experiment, leading to the longer calculated length than the measured one. In contrast, the nonlinear turbulence model predicts fairly the distribution of turbulence along the boundary region of the separation, thus generating the more reasonable separation size.

In this computation, the standard wall function was used to evaluate turbulence kinetic energy and its dissipation rate at wall based on the assumption of logarithmic velocity law. However, in the reattachment region, flow velocity would no longer obey the log-law. This may lead to larger velocity after the reattachment point in computation than in experiment as seen in Fig. 5.

(4) Secondary flow

Secondary flow is one of the most complex and distinctive features of the confluence flow. However, a correctly 3D simulation of this flow pattern is also not a straightforward work. Fig. 6 displays the cross-sectional velocity field at the position x/W = -2.00. Both the present model and the experiment show that there is a clockwise large vortex near the outer bank. Its strength and position are quite well generated with the numerical model. Comparing with the experiment, the center position of the large vortex (at about y/W = 0.8) is correctly

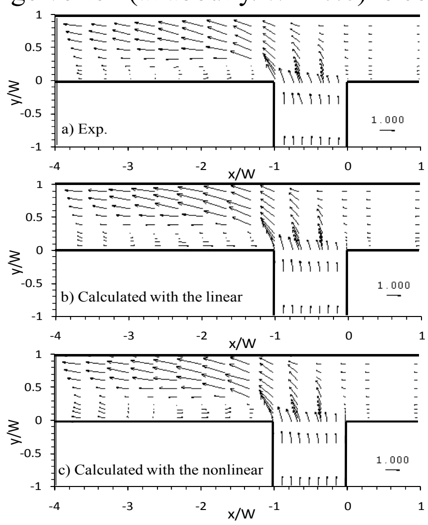

Fig. 4 Comparison of u*-v* velocity field at the surface (z/W = 0.278).

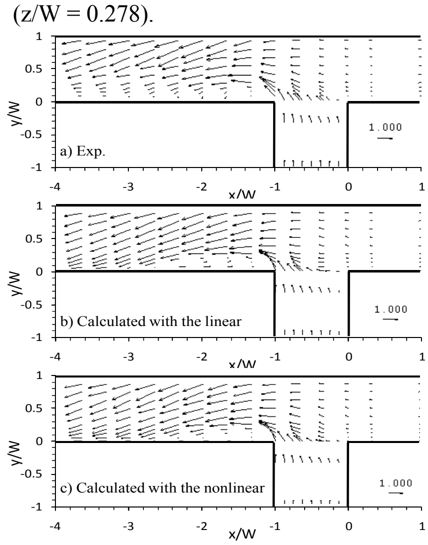

Fig. 5 Comparison of u*-v* velocity field at the bed (z/W = 0.014).

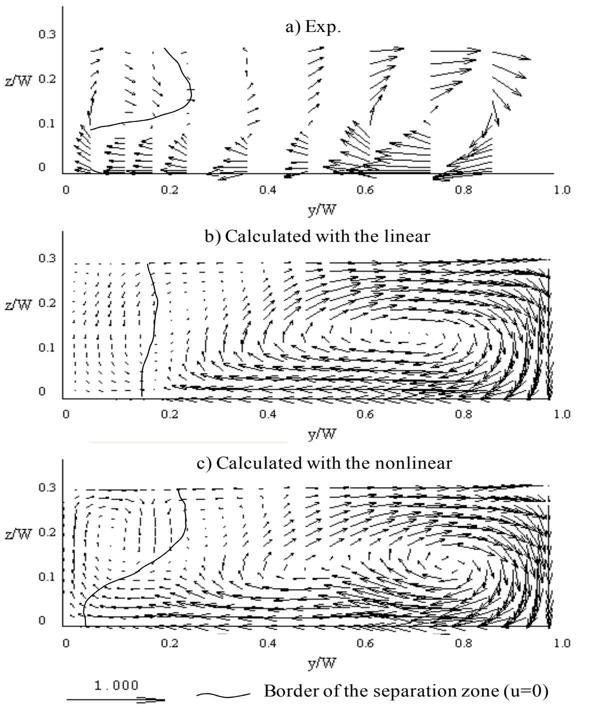

Fig. 6 Comparison of v*-w* velocity field at x/W = -2.00

predicted by the nonlinear model, while this is slightly skewed (at about y/W = 0.7) when using the linear model. At this section, the experiment also shows another clockwise small vortex near the inner bank. This important feature is not captured by the linear model. It is agreeable with the result of Huang et al.[8] at this point. The linear model, in fact, incorrectly predicts this vortex in term of its direction (anti-clockwise) and strength as seen in Fig. 6b. On the contrary, this small vortex is well reproduced by the nonlinear model as seen in Fig. 6c. The linear model does not consider the anisotropy of the Reynolds stresses, while the nonlinear one includes this aspect through the nonlinear term in Eq. (6). As seen in Fig. 6b and Fig. 6c, it can be seen that this term affects secondary current patterns, and may include the interaction between secondary current kinds. Therefore, the very good result obtained with the nonlinear model proves the important role of consideration of this aspect.

The border of the separation zone defined as the zero-velocity contour is also displayed in Fig. 6. It can be seen that comparing to the measured result, the shape of the separation along the depth is well captured with the nonlinear model. While the linear model under-predicts the dimensionless maximum width of the separation zone (0.19), the nonlinear model predicts this quantity (0.25) well in comparison with the measured one (0.26).

5. CONCLUSION

In the present paper, a 3D numerical model with the linear and nonlinear k-ε model is presented and validated in order to investigate flow features at an open-channel confluence. Based on the results obtained and discussions in the above sections, the following conclusions can be drawn:

The linear k-ε model predicts quite well the water surface mapping and velocity field. However, the model under-predicts the maximum width of the separation zone. Moreover, the turbulence kinetic energy and secondary currents are not well reproduced.

The nonlinear k-ε model performs very well and overcomes almost the limitations the linear one encounters to become the superiority over than the later. Therefore, the present 3D model with the nonlinear k-ε model is recommended to intensively investigate the confluence flow.

REFERENCES

1) Best, J. L., and Reid, I.: Separation zone at open-channel junctions, *J. Hydr. Eng.,* Vol.110(11), pp.1588-1594, 1984.
2) Gurram, S. K., Karki, K. S., and Hager, W. S.: Subcritical junction flow, *J. Hydr. Eng.,* Vol.123(5), pp.447-455, 1997.
3) Hsu, C. C., Wu, F. S., and Lee, W. J.: Flow at 90^0 equal-width open-channel junction flow, *J. Hydr. Eng.,* Vol.124(2), pp.186-191, 1998.
4) Hsu, C. C., Lee, W. J., and Chang, C. H.: Subcritical open-channel junction flow, *J. Hydr. Eng.,* Vol.124(8), pp.847-855, 1998.
5) Cheng, L., Komura, S., and Fujita, I.: Numerical simulation of the confluence flow by using k-ε models, *Ann. J. Hydrau. Engrg, JSCE*, Vol.36, pp. 169–174, 1992.
6) Dinh, T. M., Kimura, I., Shimizu, Y., and Hosoda, T.: Numerical simulation of flow at an open-channel confluence using depth-averaged 2D models with effects of secondary currents, *Journal of Applied Mechanics*, JSCE, Vol.13, pp.769-780, 2010.
7) Uchida, T. and Fukuoka, S.: A quasi-3D model using shallow water equations and horizontal vorticity equations for flows in a channel confluence, *Ann. J. Hydrau. Engrg, JSCE*, Vol.53, pp. 1081–1086 (in Japanese), 2009.
8) Huang, J., Weber, L. J., and Lai, Y. G.: Three-dimensional numerical study of flows in open-channel junctions, *J. Hydraul. Eng.,* Vol. 128(3), pp.268-280, 2002.
9) Weber, L. J., Eric, D. S., and Nicola, M.: Experiments on flow at a 90^o open-channel junction, *J. Hydraul. Eng.*, Vol.127(5), pp.340-350, 2001.
10) Kimura, I. and Hosoda, T.: A non-linear *k-ε* model with realizability for prediction of flows around bluff bodies, *Int. J. Numer. Meth. Fluids*, Vol.42, pp.813-837, 2003.
11) Ali, M. S., Hosoda, T., and Kimura, I.: A non-linear k-ε model to predict the spatial change of turbulence structures in large scale vortices, *Journal of Applied Mechanics*, JSCE, Vol.10, pp.723-732, 2007.
12) Hodges, B. R, and Street, R. L.: On simulation of turbulent nonlinear free-surface flows, *Journal of Computational Physics*, Vol.151, pp.425-457, 1999.

(Received September 30, 2010)